Structure-film thickness relationship study of sputtered NiO/Ni bilayers using depth profiling and atomic force microscopy techniques

Brian Abbey
Department of Chemistry, University of Cambridge, Cambridge, CB2 1EW, United Kingdom

John D. Lipp
CCLRC Rutherford Appleton Laboratory, Didcot, Oxon, OX11 0QX, United Kingdom

Zoe H. Barber
Department of Materials Science & Metallurgy, University of Cambridge, Cambridge, CB2 3QZ, United Kingdom

Trevor Rayment[a)]
School of Chemistry, University of Birmingham, Birmingham, B15 2TT, United Kingdom

(Received 4 October 2005; accepted 18 April 2006; published online 30 June 2006)

NiO/Ni thin film bilayers have been grown on Si (100) substrates using low temperature dc reactive magnetron sputtering. The samples were grown under identical process conditions but with different amounts of NiO deposited in order to determine film quality as a function of thickness. In order to investigate the structural properties of the NiO overlayers a synchrotron detector has been developed to make energy-resolved electron yield x-ray absorption spectroscopy measurements at ambient pressure. From these studies we have been able to construct a complete depth profile of the NiO/Ni bilayers and, by modeling of the electron multiplication/propagation processes within the films, extract quantitative information about them. In combination with atomic force microscopy measurements we have determined that there exists a clear variation in the structural and morphological properties of the NiO thin films as a function of thickness. The densest overlayers with the most conformal surface are observed for film thicknesses <20 nm and >100 nm. We rationalize these results in terms of the underlying morphology of the Ni film and the effects of misfit strain between the layers. © *2006 American Institute of Physics*. [DOI: 10.1063/1.2205556]

I. INTRODUCTION

In recent years NiO thin films have attracted particular interest due to their potential use in a wide variety of applications, for instance, as electrodes for supercapacitors[1] or as electrochromic coatings.[2] Previous studies of their structural properties, however, have mainly focussed upon films grown on single crystal substrates under highly controlled conditions such as molecular beam epitaxy[3–8] (MBE) or metal-organic chemical vapor deposition (MOCVD).[9] Films produced under these conditions lend themselves well to conventional analysis but these techniques are not ideal for high-throughput manufacturing processes. Sputter deposition offers a fast and reliable way of fabricating NiO thin films and can be easily adapted for large-area high-rate thin-film manufacture. Previous studies of the structural properties of sputtered NiO layers have used x-ray absorption spectroscopy[1,10,11] (XAS) and x-ray diffraction[12–15] (XRD) techniques to determine the effect of process parameters such as oxygen content and sputtering power upon the resulting structure of the deposited thin films. The findings on the basis of local atomic structure suggest that the films growth, structure, and optical/electrical properties depend critically upon the process conditions. In particular, as the temperature is increased (this may be achieved either by heating of the substrate during deposition or more commonly by post-growth annealing) there is a transition from a disordered nanocrystalline phase[16] to a more ordered crystalline structure.[17] However, little mention is made of the density or surface morphology of the as-deposited films and only a very few studies have investigated the correlation between these characteristics and the film thickness itself. In addition, there has been little or no analysis carried out into the structural/morphological properties of sputtered *bilayers*. The primary reason for this is likely to be the fact that it is extremely difficult to extract quantitative and meaningful data from complex systems using techniques such as high resolution x-ray diffractometry (HRXRD) where the relative roughness/inhomogeneity of each of the layers has a detrimental effect upon the quality of data that can be obtained.

In recent years we have developed a synchrotron detector capable of collecting high quality data that is insensitive to sample form,[18] which can operate at nonambient temperatures[18] and which can work in reactive gas mixtures.[19] This technique is known as ambient pressure energy-resolved electron yield XAS; the system has now evolved to the point of being a routine procedure (for the sake of brevity, hereafter we will refer to the technique as energy-resolved XAS). The underlying concept of the technique is that the Auger electrons lose energy by various inelastic processes as they propagate to a surface, and therefore the emergent electron energy profile contains information about the structure as a function of depth from the surface.

[a)]Author to whom correspondence should be addressed; electronic mail: raymentt@bham.ac.uk

Put simply, electrons emitted with energies close to the Auger energy must have originated from close to the surface, and conversely those emerging with low energy most probably originated from deep within the material. This idea has been utilized for many years in XPS and Auger electron studies of surfaces under UHV conditions.[20]

In an earlier publication on this technique[21] we showed that there were clearly visible differences in x-ray absorption spectra collected at different emitted electron energies, and while it was possible to extract the proportion of Ni and NiO contributing to the spectra it was not feasible at that time to derive a depth profile (the thickness of the NiO overlayer) from the experimental data because the data sets were limited to just two, rather-broad, electron energy ranges.

Quantitative interpretation of energy-resolved XAS measurements relies heavily upon the modeling of emission spectra. In an extensive study of total electron yield (TEY) XAS, Schröder showed that the Monte Carlo (MC) modeling could be used to simulate the trajectories of *K*-shell Auger electrons.[22–25] For a series of thermally grown NiO overlayers on Ni, reasonable agreement was observed between the fraction of NiO derived from TEY XAS data and the fraction predicted by MC modeling using NiO layer thicknesses obtained via spectroscopic ellipsometry.[23] These data confirmed the validity of MC simulations although it was noted that, in general, the NiO contribution was underestimated in the modeling studies. Using these MC algorithms a Ni *KLL* electron emission spectrum could be satisfactorily reproduced.[21,26]

Improvements made in the quality of data collection since the original publication, now make it feasible to use energy-resolved XAS measurements, in combination with MC modeling codes, to extract quantitative structural depth profiles from first principles for rough material under *in situ* conditions. In the present study we demonstrate this via an investigation of the effect of different thicknesses of NiO overlayer on the properties of NiO/Ni bilayers prepared via dc magnetron sputtering. These films have been found by XRD to be polycrystalline which is consistent with films produced under similar conditions in the literature.[14,15,27,28] By monitoring the electron-energy spectrum at each incident photon energy and grouping the corresponding extended x-ray absorption fine structure (EXAFS) spectra into eight different energy windows detailed depth profiles for the NiO overlayers have been obtained. Linear combination fitting of these spectra yields the proportion of the oxide phase present in the signal relative to the metal. The results from these studies, combined with atomic force microscopy (AFM) measurements, provide an insight into the mechanisms of growth of the sputtered bilayers.

II. EXPERIMENT

Data were collected on station 9.3 at the CCLRC Daresbury laboratory (UK) in multibunch mode with the double crystal Si(111) monochromator installed. A continuous monitoring of the incident x-ray flux was carried out using an ion chamber filled with an Ar/He mixture giving 20% transmission at the Cu edge. The x-ray beam size was 1.5 mm (height) by 10 mm (width) illuminating an area of 343.9 mm^2 with the sample kept at an angle of 2.5° with respect to the incoming x-ray beam. The detector was operated using the standard gas mixture of 75% He and 25% isobutane and operating with a drift voltage of −1500 V, a cathode potential of −560 V and with the anode held at ground.

The samples were prepared via dc magnetron sputtering from a 99.99% Ni target (Advent Research Materials Ltd.), 35×55 mm^2 in dimension. The basic bilayer structure consisted of a constant 150 nm layer of Ni covered by a NiO overlayer of varying thickness (x) deposited onto a Si (100) substrate. It is important to note that 150 nm is well in excess of the total escape depth for Ni *K*-edge Auger electrons (~100 nm).[24–26] The Ni layer was deposited in pure Ar (99.9995%, which flowed through a gas purifier), while the NiO was deposited by reactive sputtering in the presence of oxygen (using a 40% O_2/Ar gas mix). In both cases the total gas pressure was 1.7 Pa (target—substrate distance =45 mm), and the power to the target was maintained at 30 W; the deposition rate for the Ni was approximately 18 nm/min, while the NiO rate was about 5.5 nm/min. During deposition the walls of the deposition chamber were cooled with liquid nitrogen, and the substrates rested on a metal substrate support so that, with these relatively low deposition powers, we expect (from previous measurements) that the substrate temperature is maintained at approximately 0 °C.

A thorough characterization of these samples was carried out using a variety of independent techniques: x-ray reflectometry measurements were made on single layer NiO films grown on Si (100) using a Philips PW3050/65 X'Pert PRO HR horizontal diffractometer and standard XRD patterns were obtained from bilayer samples with a Philips PW1050 diffractometer. The film thickness was studied using profilometry, spectroscopic, and single wavelength ellipsometry. Profilometry was carried out using a Detak profilometer to determine the height for the NiO film, Ni film and Ni+NiO film as measured from the substrate via use of suitable masks during deposition. A Horiba-Jobin-Yvon-Uvisel spectroscopic ellipsometer operating in the energy range between 1.5 and 5 eV was used to determine the optical constants and thicknesses of the individual layers. Data was analyzed assuming a single damped Lorentz oscillator model. Single-wavelength ellipsometry (EL X-02C) was used to measure the uniformity of NiO overlayer thickness across the surface of the sample. For this method values for the refractive indices of the Ni film, NiO film, Si and native SiO layers were entered into a multilayer layer model consisting of the NiO, Ni, and substrate (defined separately as being composed of Si+2.8 nm native SiO). The values of the film thickness obtained from these three techniques were found to be in good agreement. NiO overlayer thicknesses quoted in the text are those obtained from the single wavelength ellipsometry method. For each technique at least five separate measurements were made on each sample and the standard deviation calculated. For single-wavelength ellipsometry the statistical errors were found to be less than 3%. Finally, the AFM with

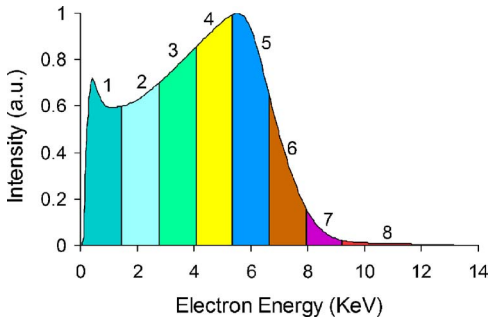

FIG. 1. (Color online) A typical PHD recorded at just above the Ni *K* edge with eight different energy regions sampled indicated.

a Dimension 3100 operating in contact mode and using the Nanoscope 4 controller was used to determine surface morphology.

III. RESULTS AND DISCUSSION

A. Energy-resolved x-ray absorption spectroscopy

1. Experimental EXAFS

Building on the experience gained from a number of previous energy-resolved XAS experiments, extremely high quality data were collected from the Ni/NiO bilayer samples. For each sample ten separate scans of ~20 min were made. The current experimental arrangement allows for the measurement of a full electron-energy spectrum at each incident photon energy. This makes it possible to achieve the maximum surface sensitivity when extracting information about the variation in composition and structure as a function of depth within a sample. By experimenting with differently sized electron-energy windows, it was found that the data sets collected from the NiO/Ni samples could be divided up into a total of eight different Auger electron-energy regions while maintaining a good signal-to-noise ratio. A typical Auger electron spectrum collected at just above the Ni *K* edge is shown in Fig. 1. The eight different energy windows within which EXAFS spectra were collected are clearly indicated.

A complete set of EXAFS spectra for one of the calibration samples is shown in Fig. 2; each of the eight spectra corresponds to a different energy window. As expected, between spectra collected at different electron energies there is a clear variation in magnitude of the sharp edge feature (at ~8340 eV) which is highly characteristic of NiO, other more subtle changes in the EXAFS can also be observed at slightly higher photoelectron energies. These changes are clear evidence of a variation in the NiO contribution to the EXAFS at different Auger electron energies. By performing a linear combination least squares fit using reference data for the pure metal and the pure oxide (also shown in Fig. 2), the oxide contribution to each of the spectra was obtained. These are shown to the right of Fig. 2.

The drop in the contribution from NiO at Auger energies greater than 10 KeV (spectra 7 and 8 in Fig. 2.) is caused by the coincidence counts. 10 KeV is greater than the Auger energy and events in this region, in principle, arise from instrumental broadening. In this circumstance, coincidence counts from more numerous low energy Auger electrons can

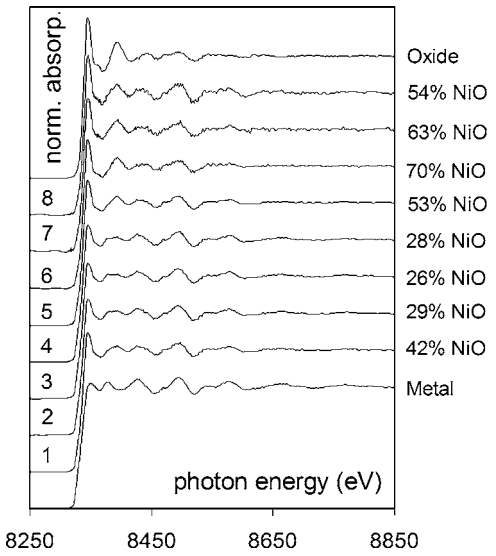

FIG. 2. Eight-EXAFS spectra corresponding to eight-different Auger electron energy windows taken from a Ni sample covered by a 40 nm NiO overlayer. The energy regions are numbered on the left hand side of the figure while the NiO contribution to the EXAFS is given down the right.

be significant. At present double counting is unavoidable when running the detector at higher rates, however, it is expected that improvements in the ability of the electronics to handle the high signal throughput would eliminate this effect altogether.

The quality of the fits may be judged from Figs. 3 and 4, which show an expanded plot of the x-ray absorption near edge structure (XANES) and the EXAFS, respectively, for the three middle energy regions (4, 5, and 6 on Figs. 2 and 3). Overlaid on these plots are the least squares fitting data, which were used to determine the phase contribution to the EXAFS arising from the oxide overlayer.

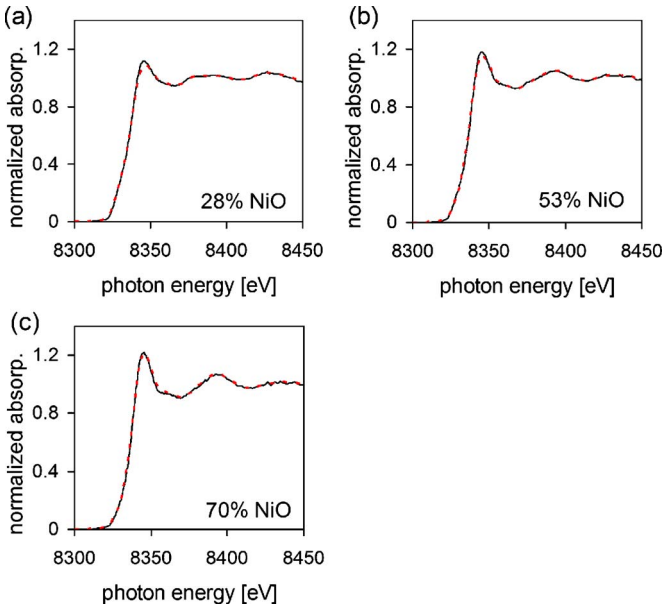

FIG. 3. (Color online) Selected background subtracted and normalized Ni *K*-edge XANES data for a Ni sample covered by 41 nm of NiO. The three different spectra correspond to three different Auger energy windows: (a) region 4, (b) region 5, and (c) region 6. The fitted profiles (broken lines) obtained by a linear combination least squares fit of the pure Ni and pure NiO data are shown for comparison.

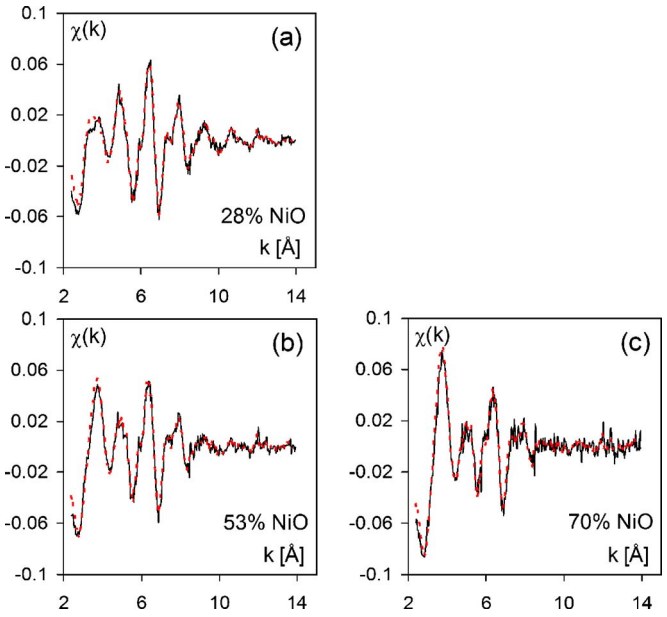

FIG. 4. (Color online) EXAFS functions $\chi(k)$ for a Ni sample covered by 41 nm of NiO for: (a) Auger energy region 4, (b) region 5, and (c) region 6. The fitted profiles (broken lines) obtained by a linear combination least squares fit of the pure Ni and pure NiO data are shown for comparison. Note the excellent quality of the fits to the experimental data.

Figure 5 shows a summary of the results of analysing the raw EXAFS data for all of the samples. The three-dimensional (3D) plot clearly shows the variation in the proportion of each phase (metal and oxide) present in the EXAFS as a function of ejected electron energy for different NiO overlayer thicknesses. It can be seen that for the Auger energies in the range of 5–10 KeV there is a rapid increase in the oxide phase contribution to the EXAFS corresponding to a concomitant improvement in the surface sensitivity of the EXAFS in this region. It is worth noting that the values for the NiO contribution in the low energy and high energy regions for the 29-nm-thick overlayer sample are in good agreement with previously published results in which only two energy regions were monitored.[21]

Of particular interest is the fact that there is an unexpected increase in the NiO contribution in the lowest energy region. Given the range of Auger energies sampled in this region the only explanation for this must be that Auger electrons from the next highest shell are contributing to the EXAFS. This is an important finding as the *L*-shell Augers have

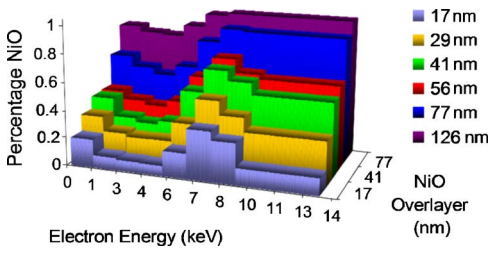

FIG. 5. (Color online) Summary of the results of analyzing the raw EXAFS data. The graph shows the variation in the contribution to the spectra from each phase present as a function of ejected electron energy. The NiO thickness for each sample is shown in the key in the top right hand corner and on the *Z* axis of the graph.

an energy which is an order of magnitude less than those coming from the *K* shell (850 and 6514 eV, respectively) and so the *L*-shell signal *must* have come from a region that is much closer to the surface (somewhat less than 10 nm). The discovery of a significant higher shell contribution to the EXAFS at lower Auger energies is only now possible because of the fact that improved instrumentation has meant that the PHD can be divided up into many different regions.

2. Determination of depth profiles by MC simulation

The earlier work of Schröder, has demonstrated that the MC electron trajectory simulations give a reliable account of the attenuation of TEY signal within a sample.[21,22,24–26] An electron energy emission spectra was available from these calculations but there was insufficient experimental data to utilize the full information inherent in the model. The availability of an experimental electron emission spectrum at each photon energy, makes it worthwhile to use the MC model to derive the relative contribution to the EXAFS signal of each phase present in the surface region as a function of the electron energy. The comparison of the experimental and calculated phase fractions would then allow the thickness of the overlayer to be determined via an iterative fitting process. The model used in the MC simulations has been previously described in detail,[23] a brief description is given below.

The Auger electron model uses single scattering MC simulations of electron trajectories to determine the probability of escape for an electron within a solid as a function of depth within the sample. One of the key requirements in the calculation of electron penetration ranges within solid materials is an accurate assessment of the electron-atom interaction cross sections. The algorithm employed within the Auger model is that developed by Browning *et al.*[29] derived using smooth empirical fits to the exact relativistic cross sections (commonly termed "Mott" cross sections) defined here as σ_{el}.

$$\sigma_{el} = \frac{3 \times 10^{-18} Z^{1.7}}{E + 0.005 Z^{1.7} E^{0.5} + 0.0007 Z^2 / E^{0.5}} \ (\mathrm{cm}^2). \qquad (1)$$

Equation (1) has the great advantage that it only contains simple powers of the electron energy E (in units of KeV). Since E is the only variable whose value needs to be updated continuously during the simulation, simple expressions of the electron energy mean that statistically significant data sets can be acquired within a very short space of time. The only other variable upon which the algorithm depends is the atomic number Z, whose value is obviously fixed for each material within the system.

Due to the drag exerted on the negatively charged electron by the positively charged nuclei surrounding it and also due to discrete inelastic scattering events such as the production of a plasmon, the electron continuously loses energy as it travels through the specimen. Ideally each energy loss would be accounted for separately by incorporating them individually into the simulation, however, because of the number of different possibilities available this is a rather lengthy and complex procedure. Instead the assumption is

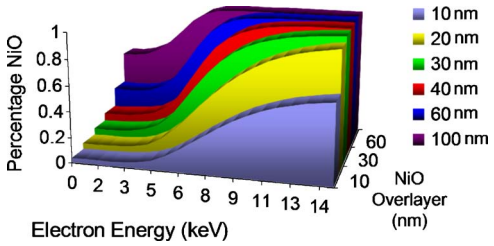

FIG. 6. (Color online) Simulated data showing the variation in the proportion of the signal from each phase present in the EXAFS as a function of ejected electron energy. The data were obtained using single scattering MC algorithms, which have been developed to simulate the path of the electrons as they propagate through the solid. Each spectrum represents the evaluation of 210 000 trajectories. The model data may be compared directly to the experimental data given in Fig. 5. Note the secondary and *L*-shell Auger contributions have been omitted from the simulation entirely.

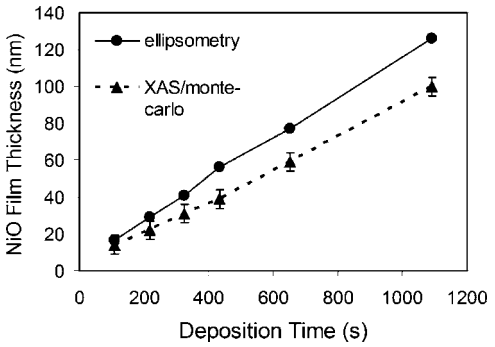

FIG. 7. Graph showing the oxide thicknesses predicted from XAS/MC simulations and the thicknesses measured directly via ellipsometry. The data are presented as a function of the NiO deposition time.

made that both the effects of electrostatic drag on the electron and the discrete energy losses incurred during inelastic scattering events may be combined and approximated by a continuous slowing down (CSD) function which gives the "stopping power" of the material in terms of energy loss dE per travelled path dl. For the current set of simulations the well known semiempirical model developed by Joy and Luo[30] (adapted from that given by Bethe in his classic 1930 paper[31]) was used.

$$\frac{dE}{dl} = -785\frac{\rho Z}{ME}\ln\left[\frac{1.166(E+0.85J)}{J}\right] \text{ (eV/Å)}, \qquad (2)$$

Where ρ is the material density (in g/cm^3) and M the atomic weight (in g/mol); J is the mean ionization potential (in eV) of the material which represents the effective average energy loss per interaction between the incident electron and the solid and is given by the expression:

$$J = 9.76Z + \frac{58.5}{Z^{0.19}} \text{ (eV)} \quad \text{for } Z > 12. \qquad (3)$$

For elements with $Z<13$ the values of J tabulated by Berger[32] were used.

Equations (1) and (2) allow for a very flexible model and are simple enough that computation times are extremely small allowing for the collection of larger data sets extremely quickly. As an example, the simulation of 210 000 Ni *KLL* electron trajectories for a 250 Å oxide overlayer thickness took a little under 15 min on a modern desktop computer. However, there are drawbacks to using such approximations, in particular, the accuracy of the CSD approximation has been shown to deteriorate as the electron energy decreases towards ~1 KeV and, by 0.8 KeV, significant differences are observed between the various different approaches available.[33,34] This is the reason why the simulated data presented here neglects the contribution from the *LMM* Auger electrons whose energy (850 eV) lies well below 1 KeV. Possible alternatives to the currently employed CSD which could be used effectively in low energy electron scattering simulations are now being examined so that the energy resolved *L*-shell contribution to the EXAFS can be accurately modeled. A summary of the results from the simulations of *K*-shell Auger electron trajectories is given in Fig. 6.

Direct comparison of the simulated data with the experimental results in the energy region between 3 and 10 KeV shows that the simulated data match very well the shape of the experimental data. In the low energy regions between 2.5 and 5 KeV the same plateau in oxide contribution is observed followed by a sharp rise in surface sensitivity of the EXAFS after ~5 KeV. Below 2.5 KeV, however, there is a clear increase in the oxide contribution in the XAS data due to contributions from the *LMM* Augers and discrete energy loss processes within the sample. This accounts for the fact that the TEY obtained from the MC algorithms tends to underestimate the NiO film thickness since *LMM* contributions are neglected in these simulations.[23] By considering the electron yield as a function of energy, it is possible to see more clearly where the strengths and the weaknesses of models of the Auger signal may lie. Thus in the case of the current data we are able to achieve improved quantification, by concentrating the analysis on the 3–10 KeV region of the Auger electron spectrum. Such an analysis also leads to an improved understanding of the factors that contribute to the electron yield. By performing an iterative comparison of the XAS to MC data, the NiO thickness which yielded the best fit between the two sets of data was obtained. Figure 7 shows the results of this comparison alongside the oxide thicknesses measured independently via a single wavelength ellipsometry.

A comparison of the predicted and measured data shows that the NiO thicknesses obtained by comparing the experimental data to the simulated give consistently lower values than the overlayer thickness measured via ellipsometry. The most probable reason for this discrepancy lies in differences in the way in which the NiO film thickness is defined for the two independent measurements. Film thickness measurements derived from EXAFS data give a measure of the *amount* of oxide present which would depend on both the density and the thickness of the overlayer. Measurements derived from ellipsometry and other surface techniques, however, give the total film thickness and do not take into account the layer density and surface roughness. Based on this hypothesis, Table I provides a list of what void fractions would be predicted by comparing the XAS/MC derived NiO thickness to the measured thickness. For the thinnest film the predicted void fraction is comparatively small (14.7%) while for the thicker films the void fraction is higher, varying be-

TABLE I. Results from a comparison of the XAS/MC derived NiO overlayer thickness to the independently measured (via ellipsometry) NiO overlayer thickness. Also shown is a summary of the quantitative data obtained from AFM analysis of the samples. The errors quoted are derived from the quality of fit between the XAS and MC data.

NiO overlayer thickness (x)		Predicted Void Fraction (%)	rms Roughness (nm)	Gaussian FWHM (nm)
XAS/MC (nm)	Measured (nm)			
14.5±1.5	17	14.7±8.8	4.18	7.88
22.0±1.5	29	24.1±5.2	4.84	11.23
31±2	41	24.4±4.9	5.16	11.06
39±3	56	30.4±4.9	4.84	10.72
59±4	78	23.4±5.2	4.63	9.72
100±6	126	20.6±4.5	4.20	8.05

tween 24% and 30%. For the very thickest films though, there appears to be a trend towards a reduced void fraction once again, dropping to around 20% for $x=126$ nm.

Based on the XAS/MC data the densest NiO films obtained by low temperature dc magnetron sputtering appear to be those with $x<20$ nm when the effects of morphology and underlying strain from the Ni layer will be most pronounced. However, due to the uncertainties associated with measurements of the void fraction (see Table I and Fig. 9) particularly in the case of the thinnest films some caution needs to be applied when drawing conclusions from this data alone. In order to obtain more direct evidence for a change in film characteristics with thickness and to rationalize the changes in density for film thicknesses >30 nm knowledge of any corresponding structural changes of the NiO thin films is needed. Section III B gives the results of an independent AFM study of the morphological properties of the NiO overlayers. Combined with the results of the XAS experiments an insight into the growth mechanism for the sputtered NiO films may be gained.

B. AFM study of NiO overlayers

In addition to studies of the internal film structure an accurate picture of the surface morphology can give an extremely good indication of thin film quality and physical characteristics. Crystallite size and homogeneity as well as surface roughness are among the parameters which are most useful when trying to characterize such structures. An AFM image of a single, 150 nm thick, sputtered layer of Ni deposited onto Si (100) (identical to the Ni layer present in the bilayers) is shown in Fig. 8(a). The average height (h) (defined here as height protruding above the sample surface rather than from the Si substrate) of the crystallites is 6.8 nm while their lateral diameter ranged from ~20–70 nm, with the majority having a diameter <40 nm. The small crystallite sizes and compact small scale structure is consistent with the fact that sputtering was carried out at ~0 °C with no postgrowth annealing,[28] thus resulting in a relatively small surface mobility for the impinging atomic species and a correspondingly large number of nucleation centers.

Figures 8(b)–8(h) show AFM images for the sputtered NiO/Ni bilayers, consisting of ~10(b), 17(c), 29(d), 41(e), 56(f), 77(g), and 126(h) nm of NiO sputtered at 0 °C onto a 150-nm-thick layer of Ni. Each sample was produced under identical conditions during the same deposition cycle. Hence the only process variable between samples is the NiO deposition time. A qualitative and quantitative analysis of the images reveals a clear variation in the surface morphology and the crystallite number density with varying overlayer thickness x. Images (b) and (c) have almost identical surface characteristics and both are similar in appearance to (a) although with slightly larger average crystallite sizes, with h equal to 8.8 and 9.6 nm for (b) and (c), respectively. Between $x \approx 30$ and 40 nm there is a rapid increase in the number of large irregular deposits of NiO which corresponds to a decrease in the crystallite number density [see histograms for Figs. 8(c)–8(e)]. These deposits are significantly larger than the smaller surface features with diameters in the range of 80–140 nm heights of ~14–25 nm. For $x\sim80$ nm [Fig. 8(g)] a significant proportion of the surface is covered by smaller scale features (those with diameter <40 nm) and for very thick overlayers ($x>120$ nm) the gaps between the large NiO deposits visible in (e), (f), and (g), are filled in by the smaller crystallites resulting in a flatter surface.

In the absence of any variation in deposition temperature or pressure between samples the observed changes in surface feature size and number density as well as surface homogeneity must arise from the differences in the thickness of the overlayer deposited onto each sample. Two factors which are of key importance in determining the final characteristics of the sample surface are the morphology of the underlying Ni layer and the defects/strain arising from the lattice mismatch between the Ni and NiO layers (~19%). Comparison of the bilayer samples to single layers of Ni and NiO grown on Si (100) substrates reveals that the surface roughness of the bilayers is dominated by the roughness of the underlying Ni layer. Essentially, a relatively "smooth" NiO layer is deposited onto a "rough" Ni surface. We can be certain of this because the rms roughness of single layers of NiO deposited onto atomically flat Si (100) substrates under identical conditions to the bilayers was between 0.2 and 1.2 nm for NiO film thicknesses in the range of 10–130 nm, while the rms roughness of the bilayer samples was between 38 and 5.2 nm (for $x=10$–130 nm). However, the surface morphology of the underlying Ni alone cannot account for the observed changes in the crystallite number density and surface characteristics of the bilayers as the NiO film develops and thickens. We therefore interpret these changes as being due to a combination of the underlying Ni morphology and the effects of lattice misfit strain.

For $x=10$ and 20 nm [Figs. 8(b) and 8(c)] the distribution of surface feature heights and morphology reveal a high number density of small features similar to that of the single Ni layer in image (a). This is consistent with the depth profile studies which predicted lower void fractions for these films. This result is not surprising if we consider that when the sputtering NiO we are depositing adatoms which have a much lower surface mobility than pure Ni because of the oxygen present in the gas mixture. In addition, due to the large lattice mismatch between the Ni and NiO layers there will be a large number of defect sites present in the thinnest

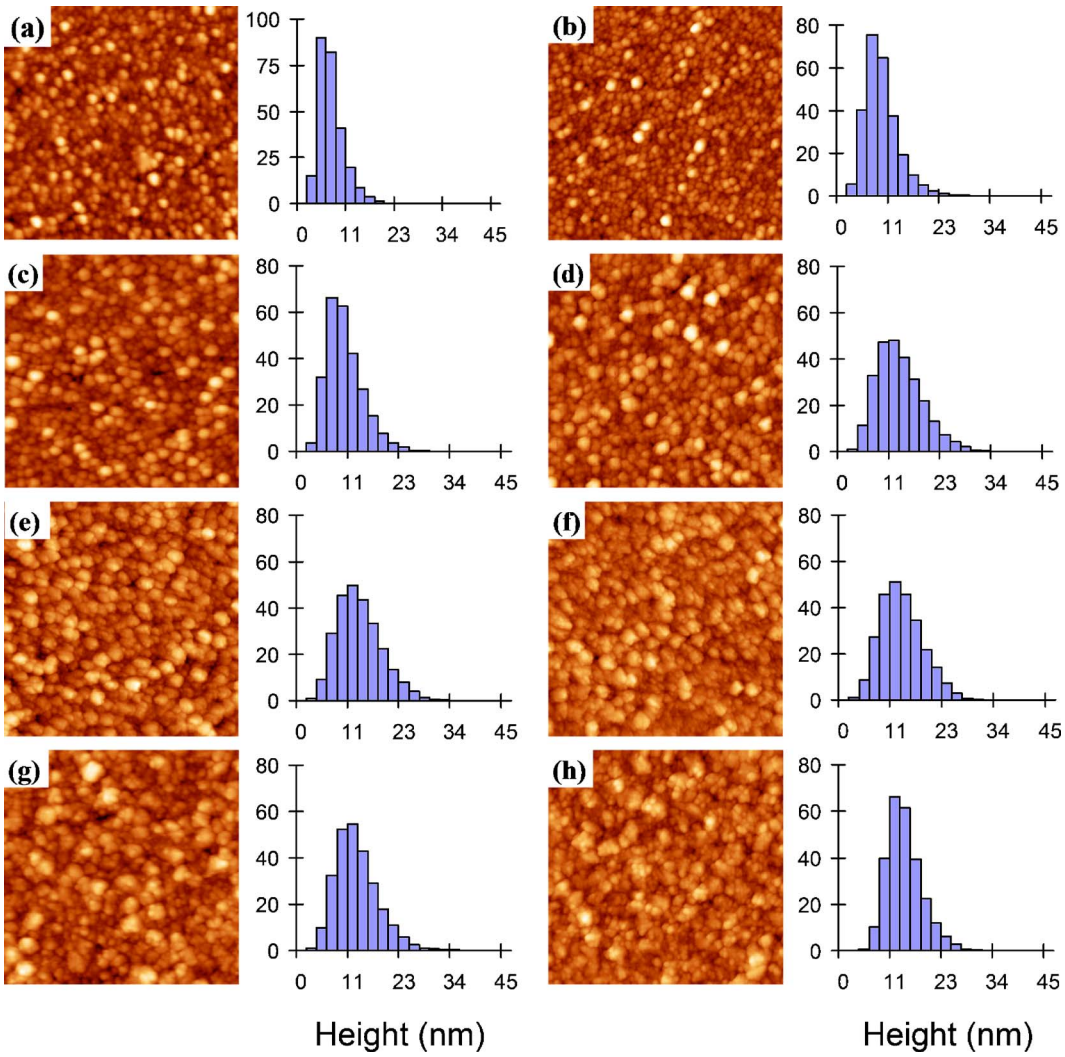

FIG. 8. (Color online) Selected contact—mode AFM images (1×1 μm^2) of the NiO overlayer surface for a series of Ni/NiO bilayer samples. (a) A single layer of sputtered Ni, (b), (c), (d), (e), (f), (g), and (h) with a NiO overlayer of ~10, 17, 29, 41, 56, 77, and 126 nm, respectively. Histograms showing the distribution of the topographical data as a function of height are shown to the right of each image. All samples were deposited at zero degrees under identical process conditions.

films, which provide a high concentration of nucleation centers. These two factors combined with the low substrate temperature mean that the surface diffusion of the adatoms is significantly inhibited for the thinnest films and so a small-crystallite compact structure closely resembling that of the underlying Ni layer results. For $x=30-60$ nm [Figs. 8(d)–8(f)] a heterogeneous mixture of large irregular islands and smaller scale features is observed as well as an overall reduction in surface feature number density. This is again consistent with the XAS/MC data that indicate a reduced density for these samples which we may now correlate to an increase in the surface void fraction. The results suggest that as the film thickens the low mobility of the adatoms leads to geometrical "shadowing"[35,36] which creates columns and voids on the surface. Also, as the film structure develops there will be fewer defect sites and hence fewer nucleation centers leading to an increase in the average feature size and a reduction in their number density.

For $x\sim80$ nm [Fig. 8(g)] there is a far greater density of small crystallites similar to those observed in single layer NiO samples grown on Si 100) (not shown here). Although there is still evidence of the previous large-scale features their surface is covered by a small-scale compact structure. This trend is even more advanced by $x=130$ nm [Fig. 8(h)] where the small crystallites have begun to fill in the spaces between the larger deposits leading to a more conformal surface and hence a reduced surface void fraction confirming the results from Sec. III B. We may interpret this as follows: as the films structure further develops and coarsens the large-scale features coalesce and to some extent "fill in" the voids between them. In addition, for the thickest films the effects of misfit strain (i.e. the creation of defects) upon crystallite nucleation will be greatly reduced meaning that growth will proceed in a similar manner to that of the single NiO layers for which a smooth conformal surface was observed. Consideration of these two factors means that we may expect the roughness features of the overlayers to become "smoothed out" once the film structure has developed sufficiently, this is what is observed directly from the AFM images.

These observations are quantified by the histograms in Fig. 8 which show the distribution of topographical events as a function of height, and by AFM measurements of the rms

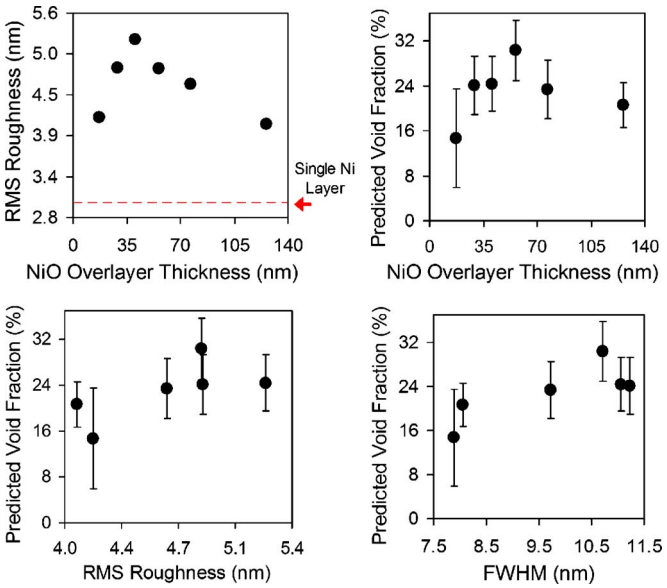

FIG. 9. (Color online) Measured rms roughness (top left) and predicted void fraction (top right) as a function of NiO overlayer thickness for a series of Ni/NiO samples. Also shown are the predicted void fractions as a function of the rms roughness (bottom left) and the FWHM (bottom right).

surface roughness. The full width at half maximum (FWHM) derived from a Gaussian fit to the histograms in Fig. 8 are summarized in Table I and Fig. 9 which also compares the topographical data to data from the XAS/MC studies.

In summary, together with the depth profile data in Sec. III A the results indicate a general trend toward lower density films as the roughness of the overlayer and the distribution of crystallites sizes increases, this occurs in the "intermediate" regime of $x=20-60$ nm. After $x\sim 80$ nm a steady improvement in the film density and surface homogeneity is observed with the surface more closely resembling that of a single thick ($\sim$130 nm) layer of NiO grown on a Si (100) substrate.

IV. CONCLUSIONS

A quantitative ambient pressure energy-resolved electron yield XAS and AFM study has been carried out upon NiO thin films deposited onto Ni via dc magnetron sputtering. Differences in the film quality have been observed as a function of the overlayer thickness. The most conformal films were found to be either those that were very thin ($<$20 nm) in which case the underlying morphology of the Ni layer was mirrored, or those that were relatively thick ($>$100 nm) in which case a morphology resembling that of a single layer of NiO sputtered onto Si was observed. The void fractions extrapolated from the XAS characterization indicate that all the thin films had a density lower than that of the bulk crystalline solid, this is consistent with the XRD data for the films and with previous studies of sputtered NiO layers both of which indicate that samples produced at lower temperatures ($<$120 °C) tend to adopt a polycrystalline structure with an expanded lattice parameter as compared to the bulk value.[10,17] It is also consistent with an analysis of the data carried out using EXCURVE which indicated a continuing Ni contribution to the EXAFS even for overlayer thicknesses $>$120 nm. The *changes* in film density as a function of overlayer thickness, however, we attribute to a varying surface void fraction caused by the different surface morphologies of the samples. These differences are most likely due to the effects of geometrical shadowing during growth and the influence of defect sites on NiO crystallite nucleation. In conclusion, ambient pressure energy-resolved electron yield XAS has been shown to be an excellent characterisation tool for performing *in situ* depth profile measurements on complex material systems. Currently energy resolved XAS represents the only way that such measurements can be made and it is hoped that the results from this research combined with the previously published data[18,19,21] will enable the technique to evolve beyond the stage of being a curiosity to potentially becoming a useful tool for a much wider scientific community.

ACKNOWLEDGMENTS

We acknowledge the staff of the Synchrotron Radiation Facility, Daresbury especially Ian Harvey, for their help and support. We also acknowledge Dr. A. Vollmer of the BESSY Synchrotron Radiation Facility, Berlin and Professor H. Weiss of the Otto-von-Guericke-Universität, Magdeburg (Germany) for design of the prototype cell and development of the data analysis software. We also acknowledge M. Vickers of the Materials Science Department, Cambridge for help with XRD and HRXRD work. Financial support of our project by the EPSRC is gratefully acknowledged.

[1] K. W. Nam, W. S. Yoon, and K. B. Kim, Electrochim. Acta **47**, 3201 (2002).
[2] J. Svensson and C. G. Granqvist, Appl. Phys. Lett. **49**, 1566 (1986).
[3] F. Muller, R. de Masi, P. Steiner, D. Reinicke, M. Stadtfeld, and S. Hufner, Surf. Sci. **459**, 161 (2000).
[4] Q. Guo, C. Xu, and D. W. Goodman, Langmuir **14**, 1371 (1998).
[5] N. Kitakatsu, V. Maurice, C. Hinnen, and P. Marcus, Surf. Sci. **407**, 36 (1998).
[6] S. Stanescu, C. Boeglin, A. Barbier, and J.-P. Deville, Phys. Rev. B **67**, 035419 (2003).
[7] A. Recnik, D. L. Carroll, K. A. Shaw, D. M. Lind, and M. Ruhle, J. Mater. Res. **12**, 2143 (1997).
[8] C. Mocuta, A. Barbier, G. Renaud, Y. Samson, and M. Noblet, J. Magn. Magn. Mater. **211**, 283 (2000).
[9] A. C. Wang, J. A. Belot, and T. J. Marks, J. Mater. Res. **14**, 1132 (1999).
[10] A. Kuzmin, J. Purans, and A. Rodionov, J. Phys.: Condens. Matter **9**, 6979 (1997).
[11] P. Luches, E. Groppo, C. Prestipino, C. Lamberti, C. Giovanardi, and F. Boscherini, Nucl. Instrum. Methods Phys. Res. B **200**, 371 (2003).
[12] K. M. E. Miedzinska, B. R. Hollebone, and J. G. Cook, J. Phys. Chem. Solids **49**, 1355 (1988).
[13] I. Hotovy, J. Huran, L. Spiess, J. Liday, H. Sitter, and S. Hascik, Vacuum **69**, 1178 (2003).
[14] I. Hotovy, J. Liday, L. Spiess, H. Sitter, and P. Vogrincic, Jpn. J. Appl. Phys., Part 2 **42**, L1178 (2003).
[15] I. Hotovy, J. Huran, and L. Spiess, J. Mater. Sci. **39**, 2609 (2004).
[16] S. Yamada, T. Yoshioka, M. Miyashita, K. Urabe, and M. Kitao, J. Appl. Phys. **63**, 2116 (1988).
[17] A. M. Andersson, W. Estrada,C. G. Granqvist,A. Gorenstein, and F. Decker,*Optical Materials Technology for Energy Efficiency and Solar Energy Conversion Ix* (SPIE-The International Society for optical Engineering, Bellingham, 1990) pp. 96–110.
[18] A. Vollmer, J. D. Lipp, H. Weiss, R. O'Malley, and T. Rayment, Angew. Chem., Int. Ed. **43**, 3691 (2004).
[19] A. Vollmer, J. D. Lipp, J. R. I. Lee, G. E. Derbyshire, and T. Rayment, Anal. Chem. **75**, 6571 (2003).
[20] G. Ert and J. Kuppers, *Low Energy Electrons and Surface Chemistry* (Wiley-VCH, New York, 1986), p. 386.
[21] T. Rayment, S. L. M. Schroeder, G. D. Moggridge, J. E. Bateman, G. E.

Derbyshire, and R. Stephenson, Rev. Sci. Instrum. **71**, 3640 (2000).
[22]S. L. M. Schröder, Solid State Commun. **98**, 405 (1996).
[23]S. L. M. Schröder, *Chemistry* (Cambridge University, Cambridge, 1996).
[24]S. L. M. Schröder, J. Phys. IV **7**, 153 (1997).
[25]S.L. M. Schröder, G.D. Moggridge, R.M. Ormerod, T. Rayment, and R.M. Lambert, Surf. Sci. **324**, L371 (1995).
[26]S.L. M. Schröder, G.D. Moggridge, R.M. Lambert, and T. Rayment in *Advances in Spectroscopy*, edited by R.J.E.C.a.R.E. Hester (Wiley, New York, 1998), p. 1–29.
[27]I. Hotovy, J. Huran, L. Spiess, R. Capkovic, and S. Hascik, Vacuum **58**, 300 (2000).
[28]H. L. Chen, Y. M. Lu, and W. S. Hwang, Surf. Coat. Technol. **198**, 138 (2005).
[29]R. Browning, T. Z. Li, B. Chui, J. Ye, R. F. W. Pease, Z. Czyżewski, and D. C. Joy, J. Appl. Phys. **76**, 2016 (1994).
[30]D. C. Joy and S. Luo, Scanning **11**, 176 (1989).
[31]H. A. Bethe, Ann. Phys. **397**, 325 (1930).
[32]M. J. Berger NBS Internal Report No. 82-2550-A (NBS, Washington, DC, 1983).
[33]T. S. Raosahib and D. B. Wittry, J. Appl. Phys. **45**, 5060 (1974).
[34]G. Love, M. G. C. Cox, and V. D. Scott, J. Phys. D **10**, 7 (1977).
[35]D. L. Smith, *Thin-Film Deposition: Principles and Practice* (McGraw-Hill, Boston, 1995).
[36]J. A. Thornton, J. Vac. Sci. Technol. **11**, 666 (1974).